Southern Hemisphere tree-rings as proxies to reconstruct Southern Ocean upwelling

5 Christian Lewis[1], Rachel Corran[1], Sara E. Mikaloff-Fletcher[3], Erik Behrens[3], Rowena Moss[3], Gordon

Brailsford[3], Andrew Lorrey[3], Margaret Norris[1], Jocelyn Turnbull[1,2]

[1]GNS Science, Rafter Radiocarbon Laboratory, Lower Hutt, New Zealand
[2]CIRES, University of Colorado at Boulder, Boulder, Colorado, USA
[3]National Institute of Water and Atmospheric Research (NIWA), Wellington, New Zealand

10 *Correspondence to*: Dr. Christian Lewis (c.lewis@gns.cri.nz)

Abstract. The Southern Ocean plays a key role in regulating global climate and acting as a carbon sink. This region, defined as south of 35°S, is accountable for 40% of all oceanic anthropogenic CO_2 uptake, and 75% of ocean heat uptake between 1861 and 2005. However, the strength of the Southern Ocean sink (air-sea CO_2 flux) is variable - weakening in the 1990s and strengthening again in the 2000s. Typical methods of constraining the flux must grapple with two opposing forces: outgassing

15 of natural CO_2 and uptake of anthropogenic CO_2. Reconstructions of atmospheric radiocarbon ($\Delta^{14}CO_2$) from Southern Hemisphere tree-rings may be a viable method of observing the one-way outgassing flux of natural CO_2, driven by Southern Ocean upwelling. Here we present more than 400 tree-ring $\Delta^{14}C$ measurements from 13 sites in Chile and New Zealand from the 1980s to the present. These measurements dramatically expand the dataset of Southern Hemisphere atmospheric $\Delta^{14}CO_2$ records. We use these records to analyse latitudinal gradients in reconstructed atmospheric $\Delta^{14}CO_2$ across the Southern Ocean.

20 Tree-rings from New Zealand's Campbell Island (52.5S, 169.1E) show $\Delta^{14}CO_2$ was on average 3.3±3.5‰ lower than atmospheric background, driving a latitudinal gradient among New Zealand sites between 41.1°S and 52.5°S, whereas samples from similar latitudes in Chile do not exhibit such a strong gradient. We demonstrate that the gradient is driven by the combination of CO_2 outgassing from the Antarctic Southern Zone (ASZ) and atmospheric transport to the sampling sites.

1 Introduction

25   The Southern Ocean (here defined as the ocean region south of 35°S) plays a critical role in Earth's climate and the balance of carbon between the ocean and atmosphere (Anderson et al., 2009; Gruber et al., 2009; Hauck et al., 2023). The region accounts for 40% of all oceanic anthropogenic CO_2 uptake, and 75% of ocean heat uptake from 1861 to 2005 (Frölicher et al., 2015; Gruber et al., 2019; Mikaloff Fletcher et al., 2006).

      The Pacific, Atlantic, and Indian Oceans all transport carbon-rich deep-waters southward, which upwell in the

30 Southern Ocean, reaching the surface south of the Antarctic convergence (Talley, 2013)and serve as an important control on pre-industrial atmospheric CO_2 (Marinov et al., 2006). As atmospheric CO_2 mole fractions have increased through the

industrial era, these waters are now a net sink for CO_2 (Gruber et al., 2019). In contrast, north of the Antarctic zone, intermediate waters that are much lower in carbon are strong sinks for atmospheric CO_2 (Gruber et al., 2023).

Southern Ocean carbon exchange is a balance between two opposing forces: release of natural carbon to the
35   atmosphere and uptake of anthropogenic CO_2 into the ocean (Gruber et al., 2019). The balance between these processes determines the net Southern Ocean carbon flux (Gruber et al., 2009). Observational methods have used atmospheric CO_2 mole fraction or oceanic CO_2 partial pressures (pCO2) to infer the net flux rate, typically in combination with atmospheric and/or ocean modelling. These observational methods of measuring Southern Ocean air-sea CO_2 flux must grapple with estimating a small difference between these two opposing forces. Additional challenges are posed by temporal and spatial variability of the
40   air-sea CO_2 flux (DeVries et al., 2017; Fay et al., 2014; Gruber et al., 2019, 2023; Peter Landschutzer, 2015; Takahashi et al., 2012) and seasonal bias toward sampling in spring and summer (Gray et al., 2018; Gruber et al., 2019; Sallée et al., 2010). These factors have led to a wide range of Southern Ocean sink-strength estimates from various methods including ground-based atmospheric measurement, ship-based hydrography, biogeochemical floats, aircraft based flux-measurements, biogeochemical models, and inverse modelling (DeVries, 2014; Fong & Dickson, 2019; Gray et al., 2018; Gruber et al., 2019;
45   Le Quéré et al., 2007; Long et al., 2021; Mikaloff Fletcher et al., 2006; Nevison et al., 2016; Sarmiento et al., 2023).

Radiocarbon analysis is a powerful tool for informing the controls on atmospheric CO_2, and may provide a new lens through which to observe Southern Ocean flux (Levin et al., 2010; Graven et al., 2012). From the 1950s until the 1980s, the radiocarbon "bomb-spike" caused isofluxes from the biosphere, ocean, and atmosphere to be in severe disequilibrium (Randerson et al., 2002; Turnbull et al., 2017; Levin et al.). However, after decades of equilibration, since the 1980s the bomb
50   spike is no longer the dominant driver of atmospheric radiocarbon-in-CO_2 ($\Delta^{14}CO_2$) variability, and the Northern Hemisphere $\Delta^{14}CO_2$ spatial patterns are primarily driven by fossil fuel emissions, while the Southern Hemisphere signature is driven by ocean exchange (Levin et al., 2010; Naegler & Levin, 2009; Randerson et al., 2002; Turnbull et al., 2009).

The ocean exchange that drives atmospheric $\Delta^{14}CO_2$ is the same that determines net Southern Ocean sink strength: outgassing of natural CO_2 versus anthropogenic CO_2 uptake. The waters transported to the Southern Ocean surface via the
55   global thermohaline circulation have distinct properties – they are oxygen poor, macronutrient and carbon rich, and old (Gray et al., 2018; Le Quéré et al., 2007; Lovenduski et al., 2008; McNichol et al., 2022; Talley, 2013). Outgassing of CO_2 from these old waters imparts a distinctly low radiocarbon signature ($\Delta^{14}C$) on the atmosphere, in particular in the Indo-Pacific Sector (Rend et al., 2022). As the atmosphere has been saturated with elevated levels of bomb-^{14}C, outgassing is measurable as a one-way flux via depletion of atmospheric ^{14}C. Long-term high-precision $\Delta^{14}CO_2$ records have detected such upwelling signals
60   (Graven et al., 2012; Levin et al., 2010). However, observation sites are limited, and many records are short or include gaps (Graven et al., 2007; Hua et al., 2021).

Here we propose that Southern Hemisphere tree-ring reconstructions of atmospheric $\Delta^{14}CO_2$ may be used to fill in these gaps and expand the available dataset. Tree-rings are considered the "gold-standard" for recording changes in atmospheric ^{14}C over long time scales (Southon et al., 2016). Tree rings are used for calibration to calendar dates via the

65   "crossdating" of rings (Leavitt & Bannister, 2009; Reimer et al., 2009, 2013; Southon et al., 2016; Stuiver & Quay, 1981) and can be used for recent carbon cycle studies via the use of the bomb-spike (Ancapichun et al., 2021; Hua et al., 2013, 2021; Turnbull et al., 2017). While a powerful method, users must beware of pitfalls (Leavitt & Bannister, 2009; Southon et al., 2016) including potential interlaboratory offsets, and missing or false rings (Hua et al., 2021; Turnbull et al., 2017), growing season uncertainty or incorporation of carbon from previous or following growth years. We address these concerns in our

70   methodology.

         In this paper, we present a time-series of 438 tree-ring Δ^{14}C measurements from 13 sites in Chile and New Zealand from 1980-2016. We use several different methods to ensure that the ring counts are correct, and also test that sites are representative of ocean signals. We compare these tree ring Δ^{14}C measurements to a smoothed long-term record of Southern Hemisphere atmospheric Δ^{14}C from Baring Head and Cape Grim (Levin et al., 2010; Turnbull et al., 2017), calculating $\Delta\Delta^{14}$C.

75   We find that tree-ring $\Delta\Delta^{14}$C from New Zealand sites have a strong relationship with latitude (lower $\Delta\Delta^{14}$C found further south). Atmospheric back-trajectory modelling is used to estimate origins of air masses arriving at each tree-ring site and examined in context. We link air-mass origins with GLODAP surface ocean DIC Δ^{14}C measurements and polar frontal zone spatial extents. We find that low $\Delta\Delta^{14}$C at our southernmost New Zealand site (Campbell Island) is driven by air originating in the Indian Sector of the Antarctic Southern Zone which exhibits near year-round outgassing (Gray et al., 2018) with lower

80   surface ocean DIC Δ^{14}C than the Pacific Sector. This work focuses on establishing the method of using Southern Hemisphere tree-ring Δ^{14}C measurements as a proxy for Southern Ocean upwelling, and does not focus on temporal trends, which will be addressed in a following work.

2 Methods

2.1 Tree-ring sampling, measurement and ring count validation

85

         Tree-ring sampling in New Zealand and Chile was conducted during field campaigns in 2016 and 2017. The west coasts of Chile, New Zealand and New Zealand's Subantarctic islands were selected because of the predominant westerly air-flow which has ocean-influence and minimal terrestrial biosphere or anthropogenic influence (Fig 2 a/b, Table 1).

Country	Site	Lat	Lon	Species	Ring Code
Chile	Bahia San Pedro	-40.9	73.9	Podocarpus nubigenus (mañío macho)	BSP-T1-C2
Chile	Bahia San Pedro	-40.9	73.9	Notofagus betuloides (coigue)	BSP-T2-C1
Chile	Tortel River	-47.8	73.6	Notofagus betuloides (coigue)	TOR-T6-C1
Chile	Tortel Island	-47.8	73.6	Notofagus betuloides (coigue)	TOR-T4-C1
Chile	Seno Skyring	-52.5	72.1	Notofagus betuloides (coigue)	SKY-T3-C1/SKY-T4-C2
Chile	Monte Tarn, Punta Arenas	-53.7	71	Pilerodendrum wiferum (male spruce)	TAR-T3-C1
Chile	Monte Tarn, Punta Arenas	-53.7	71	Notofagus betuloides (coigue)	TAR-T6-C2
Chile	Puerto Navarino, Isla Navarino	-54.9	68.3	Notofagus betuloides (coigue)	PNV-T1-C1
Chile	Baja Rosales, Isla Navarino	-54.9	67.4	Notofagus betuloides (coigue)	ROS-T1-C1/ROS-T4-C1
New Zealand	Baring Head, NZ	-41.1	174.1	Pinus radiata (radiata pine)	BHD-T1-C1/BHD-T1-C3
New Zealand	Eastbourne 1/Eastbourne 2	-41.3	174.1	Agathis australis (kauri)	NIK19-T1-C2/ NIK23-T1-C2
New Zealand	Haast Beach	-43.9	169	Pinus radiata (radiata pine)	HAB-T1-C1/ HAB-T1-C2
New Zealand	Oreti Beach	-46.4	168.2	Pinus radiata (radiata pine)	ORT-T2-C1/ORT-T2-C2
New Zealand	Campbell Island	-52.5	169.2	Picea sitchensis (sitka spruce)	WLT-T2-C2/WLT-T3-C3

90 **Table 1. Tabulation of site names, latitude & longitudes, species, and ring-codes of trees that were selected and cores that were used in the final work. The final column references numbered locations on Figure 2a/b maps.**

Traditional dendrochronology requires multiple trees within a stand of forest for reliable chronologies from annual growth rings. In this work, trees within stands were deliberately avoided in exchange for isolated specimens, often a few meters

95 from the coast or on clifftops directly sampling ocean air, and avoiding the potential for reassimilation of respired CO_2 within the canopy. Trees were selected based on location close to the coast with minimal local land influences, feasibility of sampling (clear access to trunk and stable ground), clear and consistent rings and consistency of species across multiple sites.

In short, cores were taken using a 4.3mm increment corer (Haglöf Sweden), removed from the corer and stored in straws to avoid damage during moving or storage. Tree cores were brought back to the Rafter Radiocarbon Laboratory (RRL)

100 for sample workup and measurement. Cores were mounted onto aluminium foil coated cardboard with rubber bands, avoiding the glue traditionally used in dendrochronology. Only cores with clearly defined rings and unambiguous ring counts were considered for further analysis. These cores were sliced into single rings. All cores were sliced by a single person to ensure that any human bias in determining ring boundaries is consistent across all cores sampled in this study.

Sampled rings were then sliced longitudinally into thin "matchsticks" using a scalpel blade. They were then solvent-

105 washed prior to cellulose extraction using hot acidified $NaClO_2$ followed by sodium hydroxide washes under a nitrogen atmosphere followed by a final acid wash (Norris, 2015; Corran, 2021). It has been demonstrated that this technique is sufficient to remove non-cellulosic material, whereas less rigorous techniques are not (Hua et al., 1999; Norris, 2015). Samples were combusted by elemental analyser or sealed tube combustion (Baisden et al., 2013), IRMS $\delta^{13}C$ measurements were made on a subsampled aliquot of the resultant CO_2 gas and the remaining CO_2 was graphitised (Turnbull et al., 2015) prior to ^{14}C

110 measurement made on our XCAMS system (Zondervan et al., 2016). Standardisation is via Ox-I (Stuiver and Polach, 1977).

Results are reported as $\Delta^{14}C$ (Stuiver and Polach 1977), corrected for decay according to the estimated middle date of each ring growth period. In the Southern Hemisphere where the growth period spans two calendar years, dendrochronologists assign the ring year as the year that growth started, but the average age of the ring is estimated as January

4

1st of the following year for the purposes of radiocarbon decay correction. Uncertainties are determined from the AMS
counting statistics and the repeatability of replicate measurements of the tree ring samples, and is typically 2‰.

Ring counts must be validated to ensure proper chronologies and accurate interpretation of results; this is particularly
important since the expected latitudinal gradients are of similar magnitude to the annual $\Delta^{14}CO_2$ trend. We primarily validated
ring counts by $\Delta^{14}C$ bomb-spike matching: the rapid changes in $\Delta^{14}C$ during the bomb-spike are so much larger than the spatial
variability that a ring count error of a single year is immediately apparent (Andreu-Hayles et al., 2015). Miscounted rings were
easily identified by comparing measured $\Delta^{14}C$ to the Baring Head record (examples found in Supplementary Material). Where
a ring miscount was identified by this method, we discarded that core from further analysis. Where we were unable to obtain
tree cores from a given site that are long enough to include the bomb-spike, ring counts are validated through duplicate
sampling and cross-referencing $\Delta^{14}C$ measurements. Further information regarding ring-count validation can be found in the
Supplementary   Material.

2.2 **Development of background reference**

To put the tree-ring measurements into context, they are analysed relative to Southern Hemisphere atmospheric
background $\Delta^{14}CO_2$ from long term measurements at Baring Head, New Zealand (GNS/NIWA) (Turnbull et al., 2017), and
Cape Grim, Tasmania (University of Heidelberg)(Levin et al., 2010), each described below.

The Baring Head/Wellington record is the longest-running $\Delta^{14}CO_2$ dataset in the world, and the only direct Southern
Hemisphere atmospheric record to capture the ^{14}C "bomb-spike". Beginning in 1954, this record has seen changes in methods
and sampling sites over the years, discussed in detail in (Turnbull et al., 2017). There is additional noise in the record starting
from 1995 when RRL switched methods of $\Delta^{14}C$ measurement from gas-counting to AMS. In 2005, online ^{13}C measurement
allowed for appropriate fractionation correction, and reduction in this noise (Turnbull et al., 2017; Zondervan et al., 2015).
Data in the period between 2009 and 2012 also is significantly offset from the time-series, which is thought to be due to
changes in NaOH absorption sampling techniques during this period. These two periods (1995-2005; 2009-2012) are therefore
removed from the Wellington Record (Fig 1 (b)).

The University of Heidelberg Institute of Environmental Physics operates a network of time-series stations measuring
$\Delta^{14}CO_2$ sampled using the NaOH absorption method (Levin et al., 2010) and analysed via decay counting (Kromer & Munnich,
1992). The Cape Grim, Tasmania station (CGO; 40.68S, 144.68E, (Levin et al., 2010)) is at a similar latitude to Wellington,
and has data available between 1987 and 2018, overlapping the Baring Head record from 1987-2016 (Fig 1 (a/b)).
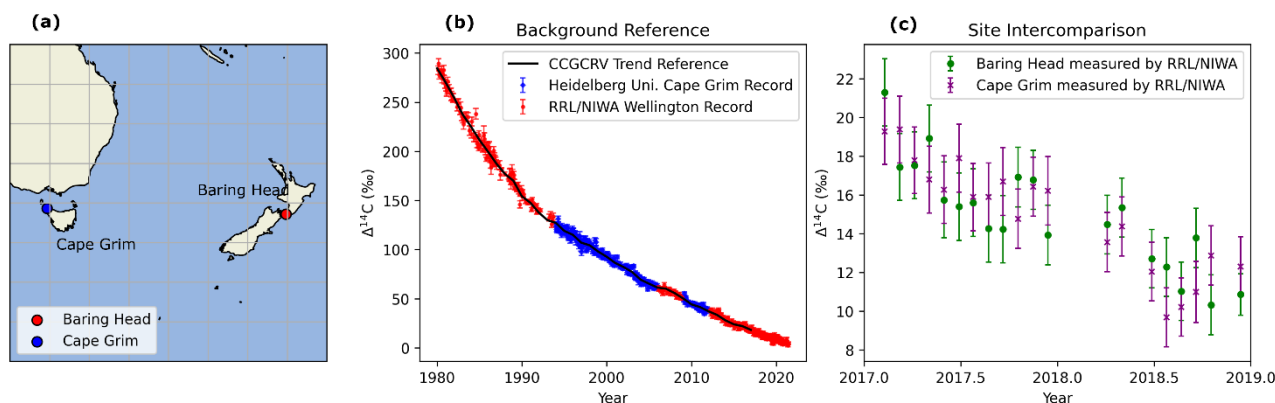
Figure 1: (a) Locations of Southern Hemisphere atmospheric background records; Cape Grim, Tasmania and Baring Head, Wellington, New Zealand. (b) Atmospheric $\Delta^{14}CO_2$ measured at Baring Head and Cape Grim post-1980. Certain periods of data have been removed, see Methods. (c) Comparison of $\Delta^{14}CO_2$ measured at the two sites by the same laboratory to identify potential spatial driven offsets in atmospheric background. None were found.

The two time-series' from Baring Head and Cape Grim are combined to fill gaps that exist in both records. Two issues that arise are 1) site-site offsets and 2) $\Delta^{14}C$ measurement offsets. Justification for the merging of two datasets from different sites are 1) Cape Grim and Wellington observe air masses of similar origin (Ziehn et al., 2014), and 2) a two year site-site intercomparison in which air collected from Baring Head and Cape Grim were both processed and measured at NIWA/GNS found no measurable difference between the sites (Fig 1 (c)). Comparability between $\Delta^{14}C$ measurements at RRL and Heidelberg University is within goals re-established by the WMO and GGMT in 2020 (0.5‰) (Crotwell et al., 2020). The merged dataset will subsequently be referred to as the "Southern Hemisphere Background" or SHB.

2.3 Interfacing Samples with Reference Dataset

The merged SHB contains discrete temporal values (sampling dates/times), representing the date a whole-air flask sample was collected, or the median sampling date for passive NaOH absorption. The tree-ring $\Delta^{14}CO_2$ data has time values set to January 1st (summer) of the growth year. In order to estimate the difference between tree-ring $\Delta^{14}CO_2$ and SHB, the time axis of both datasets must be matched.

We use the NOAA Global Monitoring Laboratory's CCGCRV curve fitting method (Thoning et al., 1989) to interpolate and smooth the SHB for comparison with the tree-ring $\Delta^{14}CO_2$, using a FFT filter cut-off of 667. The goal is to reduce the noise associated with the relatively large uncertainties on individual $\Delta^{14}C$ measurements, which can result in a single outlier $\Delta^{14}C$ measurement in the SHB record aliasing into a deviation in $\Delta\Delta^{14}C$ in all the other records. Uncertainties on the smoothed, interpolated data are obtained using a Monte Carlo scheme run to 10,000 iterations (Turnbull et al., 2017; Hua et al., 2021). More information about this scheme can be found in the Supplemental Material. The mean of the SHB smoothed data for October to March is used for comparison with the tree-ring $\Delta14CO_2$. Taking the difference between tree-ring $\Delta^{14}CO_2$ and the "trended" SHB yields $\Delta\Delta^{14}CO_2$ (Eq. 1). Data will be included in Supplementary Material.

$$\Delta\Delta^{14}CO_2 = \Delta^{14}CO_{2\_TreeRing} - \Delta^{14}CO_{2\_SHB} \qquad\qquad (1)$$

170

2.4 Sampled Time Period

While the tree-ring records in some cases extend back to <1950, and we measured some tree rings from the initial bomb-spike to validate the ring counts, this study focuses on the "Post-bomb period" from 1980's to the present (Turnbull et al., 2016). After the thermonuclear weapons testing created the radiocarbon "bomb-spike", isofluxes (differences between reservoir and

175 atmosphere) from the terrestrial biosphere and the ocean to atmosphere were strongly negative, as the systems were in severe disequilibrium (Levin et al., 2010; Naegler & Levin, 2009; Randerson et al., 2002; Turnbull et al., 2016). We select our samples post-1980 when equilibrium was closer to being established, the sign in biosphere isoflux had changed to positive, and the fossil fuel and ocean signals become the dominant drivers of $\Delta^{14}C$ spatial variability (Levin et al., 2010; Naegler & Levin, 2009; Randerson et al., 2002; Turnbull et al., 2016). Biosphere respiration of bomb ^{14}C now had higher $\Delta^{14}C$ than the atmosphere,

180 while the oceans still have a $\Delta^{14}C$ lower than the atmosphere, with the possible exception of some tropical regions (Graven et al., 2012). Fossil fuels always have strongly negative isofluxes, essentially diluting atmospheric ^{14}C (Suess 1955; Turnbull et al., 2016; however, in this Southern Hemisphere study we aim to avoid local fossil-fuel contribution.
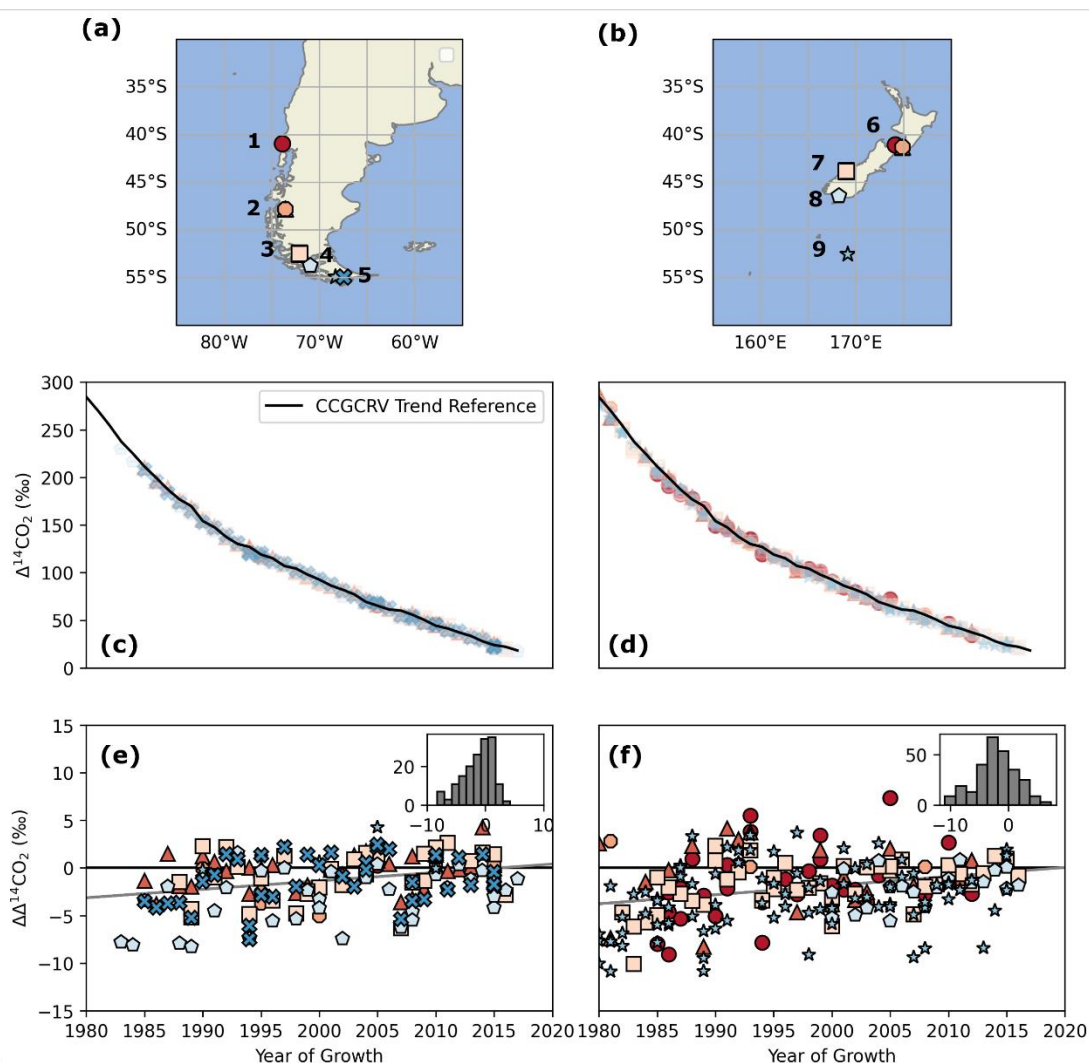
Figure 2: (a) and (b) show the sampling sites in Chile and New Zealand. Numbers refer to stations as follows: 1) Bahia San Pedro, 2) Tortel River & Tortel Island 3) Seno Skyring 4) Monte Tarn, Punta Arenas, 5) Puerto Navarino & Baja Rosales, Isla Navarino 6) Baring Head & Eastbourne, 7) Haast Beach, 8) Oreti Beach, 9) Campbell Island. (c) and (d) show the measured $\Delta^{14}CO_2$ values overlaid on the Southern hemisphere background. (e) and (f) show the difference between tree ring $\Delta^{14}CO_2$ and the Southern Hemisphere Background ($\Delta\Delta^{14}CO_2$). Inset histograms reflect all data from respective continents binned into 10 equal bins.

2.5 Atmospheric Back-Trajectories

We use the NOAA HYSPLIT air parcel trajectory model (https://www.arl.noaa.gov/hysplit/) to estimate the source regions of air parcels arriving at each sampling site. We determined mean back-trajectories by running HYSPLIT in backwards mode for with starting trajectories once every two days for the three months through the height of the growing season, running backwards in time for six days (December, January, February) for selected years during which meteorological data was

8

available. Years 2005-2006, 2010-2011, 2015-2016, and 2020-2021 were selected. For each site, 185 trajectories were produced. This number of trajectories was selected to give a reasonable representation of the air mass origins over the full time period, while balancing the computational effort required. Results are presented as a heat-map showing the distribution
200   of points over the trajectories. HYSPLIT was run via the Python PySPLIT package (Warner, 2018).

Back-trajectories are analysed to understand the general direction of air origin, and also potential influence of biosphere or fossil fuel $\Delta^{14}CO_2$ influences.

Air mass back-trajectory results are analysed in context to previously constrained Southern Ocean "fronts" (Orsi, 1995). We will refer to the zones in between the fronts similar to (Gray et al., 2018): the subtropical zone (STZ), subantarctic
205   zone (SAZ), polar frontal zone (PFZ), Antarctic-Southern Zone (ASZ), and Seasonal Ice Zone (SIZ).

2.5 GLODAP Ocean ^{14}C data

The GLODAP Merged and Adjusted Data Product v2.2023 is used to add context to the discussion of our results (Key et al., 2004; Lauvset et al., 2023; Olsen et al., 2016). The data was filtered for existing radiocarbon measurements ('G2c14') south of
210   5°S, shallower than 100m, and post-1980 to match our tree-ring temporal span. Frontal zones from (Orsi, 1995) were interpolated to distinct longitude values of samples in the dataset, to allow comparison of the sample latitude to front latitudes. Then, each measurement was "binned" in one of the Southern Ocean frontal zones, and either Pacific or Indian Ocean, based on bottle latitude/longitudes. Further details on interpolation are included in the Supplementary Materials. The Pacific sector is defined as between 120°E to 70°W, and the Indian sector is between 21°E and 120°E. The mean and standard deviations for
215   nitrate and Δ^{14}C, by ocean sector (and total ocean), for each polar frontal zone are shown in Figu 6 (c) and (d), and tabulated in the Supplementary Materials.

3 Results and Discussion

$\Delta^{14}CO_2$ measurements from each site are overlaid with SHB (Fig 2 c/d) to show an overview of the data. All records reflect the general long-term pattern of decreasing $\Delta^{14}CO_2$ that is observed in the SHB record and globally. Small deviations
220   from the SHB record become apparent when $\Delta\Delta^{14}CO_2$ is calculated for each site (Fig 2 (e/f)). The inset histogram shows the distribution of all data from the New Zealand or Chilean sector. The most prominent feature of Fig 2 (e/f) is the year-to-year variability at all locations, likely driven by a combination of interannual variability in oceanic ^{14}C fluxes, atmospheric transport, and tree growth periods. This manuscript intends to evaluate latitudinal gradients only. Temporal trends will be discussed further in a companion manuscript. Raw $\Delta^{14}CO_2$ data (Fig 2(e/f) are not temporally de-trended before means are taken (data in
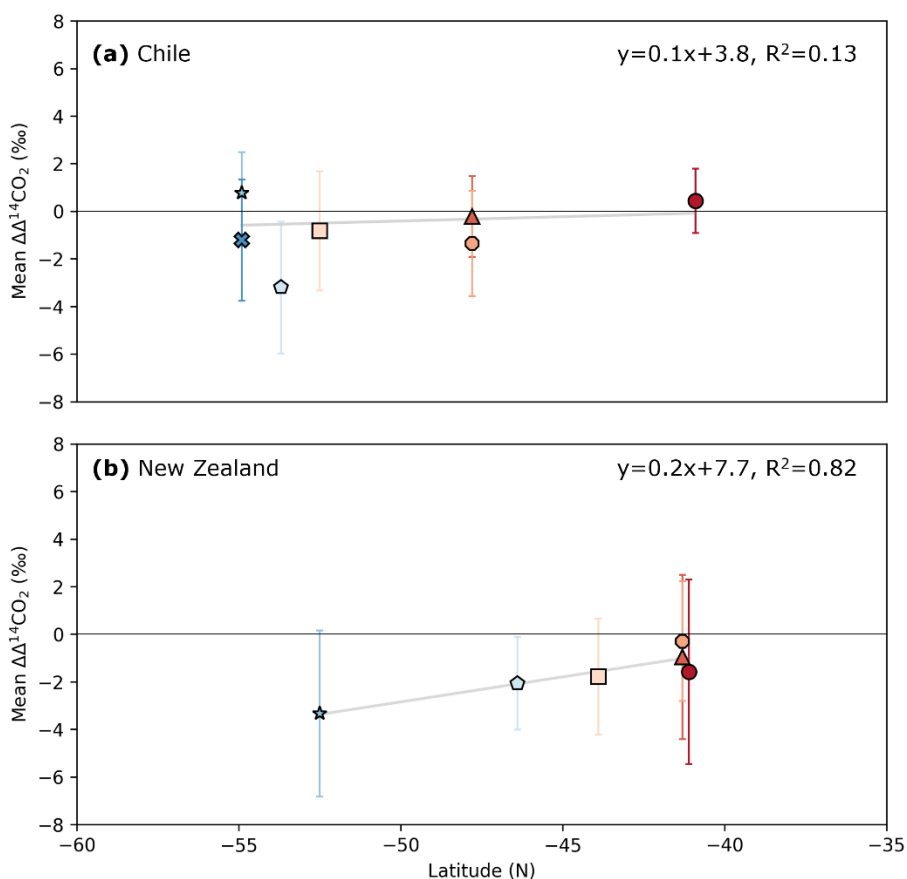225   Fig 3).

230

Figure 3: Mean $\Delta\Delta^{14}CO_2$ value for each individual site in (a) Chile and (b) New Zealand. Symbols and colors correspond to Fig 2. Error are propagated throughout the analysis.

3.1 New Zealand Sites

235   The mean and standard deviation of $\Delta\Delta^{14}CO_2$ for each site over the record is shown in Fig 3. The colors and symbols correspond to Fig 2. The three sites at or near Baring Head (origin of background record) (Fig 3(b)) are close, but not identical, to SHB. Tree rings incorporate air over a months-long growing season regardless of wind-direction, while individual measurements used for SHB are either a temporal snapshot (air flask sample) or a two-week integration (NaOH absorption). This difference is a likely driver of such variability.

240   All New Zealand sites' $\Delta\Delta^{14}CO_2$ means are within 1-σ of 0‰. Nonetheless, there is a linear trend ($R^2 = 0.82$) and steep slope compared to that of Chilean sites (0.21‰/°Lat vs 0.09‰/°Lat). This slope is driven by our southernmost New Zealand site, Campbell Island, with lowest mean $\Delta\Delta^{14}CO_2$ (-3.8 ± 3.0‰).

Results from HYSPLIT back-trajectories are displayed as heatmaps for selected sites in Fig 4, with remaining sites shown in the Supplementary Material. Heatmap data is also displayed as a bar chart in Fig 5, with a table in the Supplementary

245   Material. Campbell Island is the only New Zealand site where the HYSPLIT back-trajectory plume core sits in the SAZ. HYSPLIT modelling indicates that air moving toward Campbell Island spent the most amount of time in both the PFZ and ASZ (15.3 and 24.4%; Figure 5). Most Southern Ocean outgassing occurs in these two zones, with the latter showing near year-round outgassing (Gray et al., 2018).
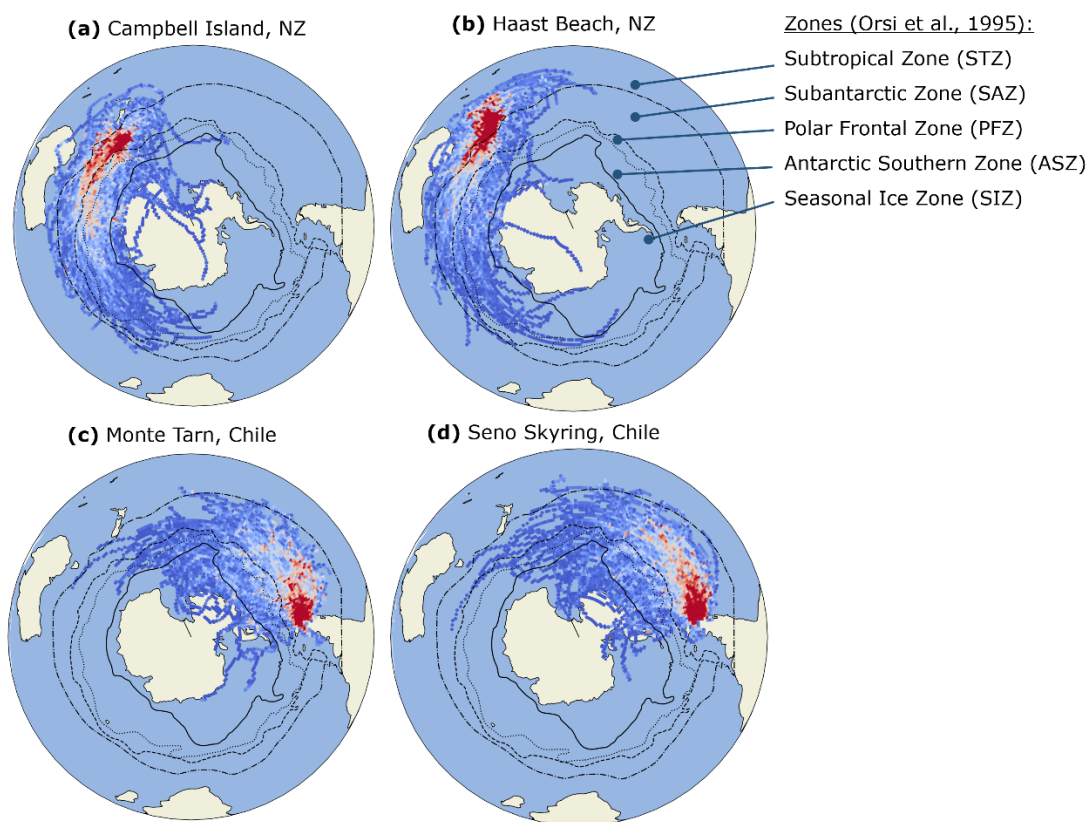
Figure 4: HYSPLIT back-trajectories shown for select sites. Trajectories for all other sites are found in Supplementary Material.
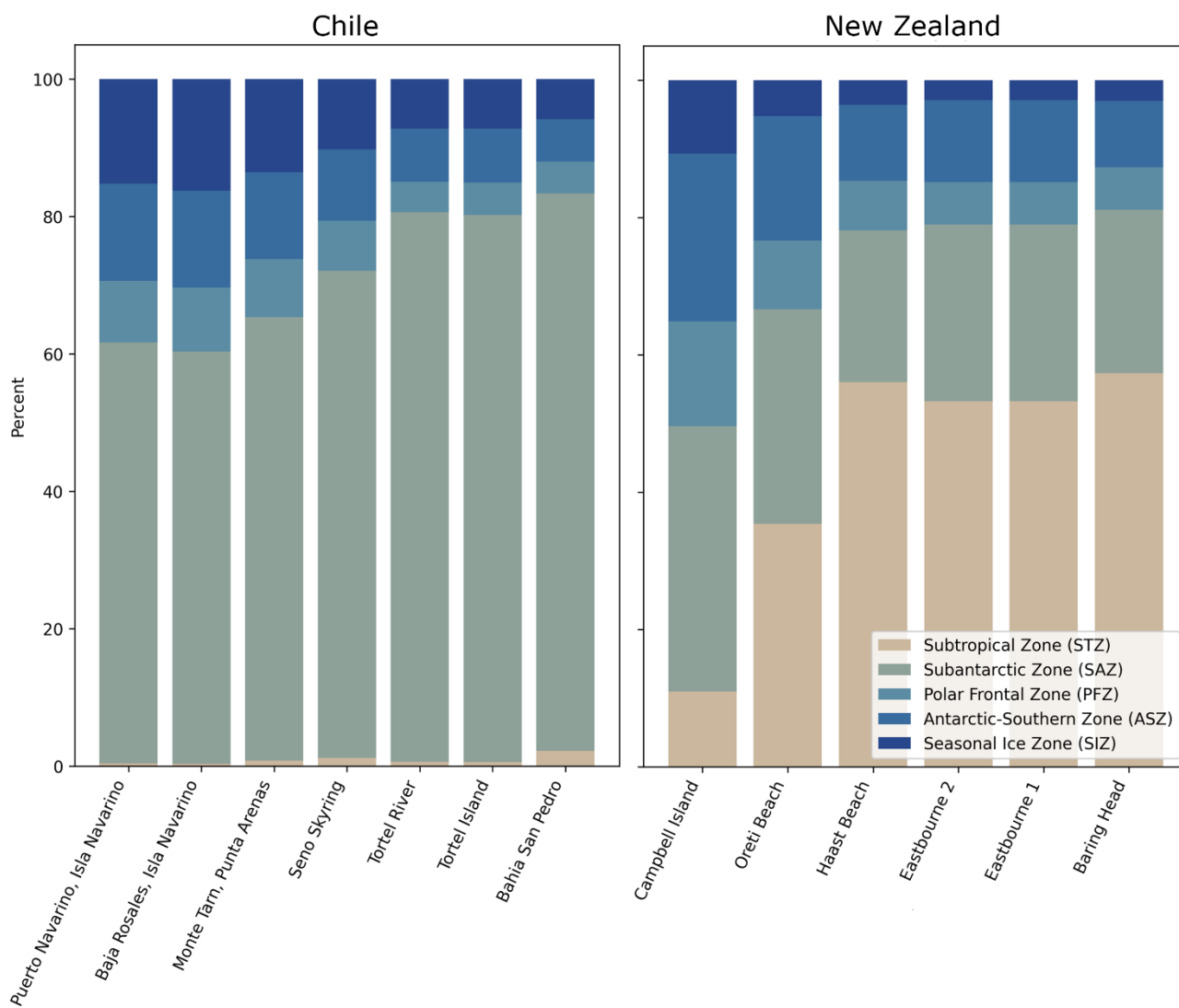
Figure 5: Visual representation of the amount of time HYSPLIT back-trajectories from each site spend in each
260 **Southern Ocean frontal zone. The Polar Frontal Zone, Antarctic Southern Zone and Seasonal Ice Zone are opaque to highlight these regions influence on Southern Ocean outgassing.**

Figure 6 shows nitrate and DIC Δ^{14}C from GLODAP (see Methods). Nitrate increases and DIC Δ^{14}C values decrease toward higher latitudes into the PFZ, ASZ, and SIZ. DIC Δ^{14}C decreases by ~150‰ between the STZ and ASZ. These are

265   distinct markers not only of Southern Ocean upwelling but of the low $\Delta^{14}C$ values imparted from old surface water masses to overlying air-masses carried on to our tree-ring sites.

We hypothesize that the New Zealand $\Delta\Delta^{14}CO_2$ latitudinal gradient is driven by Southern Ocean outgassing in the PFZ and ASZ which feed air to Campbell Island in greater abundance relative to more northern sites. Campbell Island tree-rings may therefore be useful for detecting changes in outgassing in the Indian Ocean sector of the Southern Ocean PFZ and ASZ.

270   **3.2 Chilean Sites**

A weak latitudinal gradient exists in the Chile dataset; however, this is driven by one site (Monte Tarn; 53.7°S). Excluding this site, all means are indistinguishable from SHB, and the linear regression slope falls from 0.09 to 0.03, and R^2 from 0.13 to 0.05. Monte Tarn has the lowest mean $\Delta\Delta^{14}CO_2$, is the only site outside 1-σ of the SHB (mean= −3.2 ± 2.7‰) and, notably, is not the most southerly Chilean site. It is also shrouded by the mountainous barrier island Isla Clarence, and is

275   nearby a shipping lane leading to Punta Arenas. Sites in this study were specifically chosen on western coastlines to maximize the amount of clean ocean-air originating from predominant westerlies around the ACC. This makes the likelihood of fossil fuel CO_2 incorporation into the tree-rings low. Fossil CO_2 incorporation would lower $\Delta\Delta^{14}C$ in Monte Tarn tree rings; however, it is difficult to compose an estimate of the magnitude due to the privacy of shipping data.

Our southernmost Chilean records are two sites on Isla Navarino at the same latitude of 54.9°S. Of the two, Puerto Navarino

280   lies further west and is in proximity to the Argentinian city of Ushuaia, while Baja Rosales is 0.9° to the east. These two sites were selected with the expectation that any significant land biosphere signal or fossil fuel emissions from urban influence would lead to measurable differences between the two sites. However, no statistically significant offset is found between them (see Supplemental Material). Mean $\Delta\Delta^{14}CO_2$ of both sites are within 1-σ of zero (Puerto Navarino: 0.7± 1.7‰; Baja Rosales: -1.2±2.5‰).

285   **3.3 Ocean Sector Influence on Atmospheric $\Delta^{14}CO_2$**

We hypothesize that steeper latitudinal gradients are found in New Zealand versus Chilean sites due to variability in the spatial extent of Southern Ocean zones in the Indian and Pacific Oceans, and differences in $\Delta^{14}C$ values of DIC upwelling in the ASZ in the Indian versus Pacific sectors.

Hypothetically, if the amount of CO_2 originating from the same proportion of high-latitude Southern Ocean zones

290   (SIZ, ASZ, PFZ) to Chile and New Zealand were equal, it is reasonable to assume that our method should find the same gradient in $\Delta\Delta^{14}CO_2$ with latitude for Chile and New Zealand tree-rings. The Indian and Pacific sectors jointly dominating Southern Ocean outgassing, with the Pacific specifically dominating in the PFZ (Prend et al., 2022). The Pacific also has higher DIC and lower O_2 concentrations in Indian Pacific Deep Waters, which upwell around the ACC band (Chen et al., 2022), suggesting it is more carbon rich and older. Despite this, we find a stronger outgassing influence in New Zealand, which

295   lies east of the Indian Ocean. This discrepancy is especially prominent if the Chilean site Monte Tarn is excluded due to its

proximity to a shipping lane, leaving Campbell Island with the lowest $\Delta\Delta^{14}CO_2$ value.
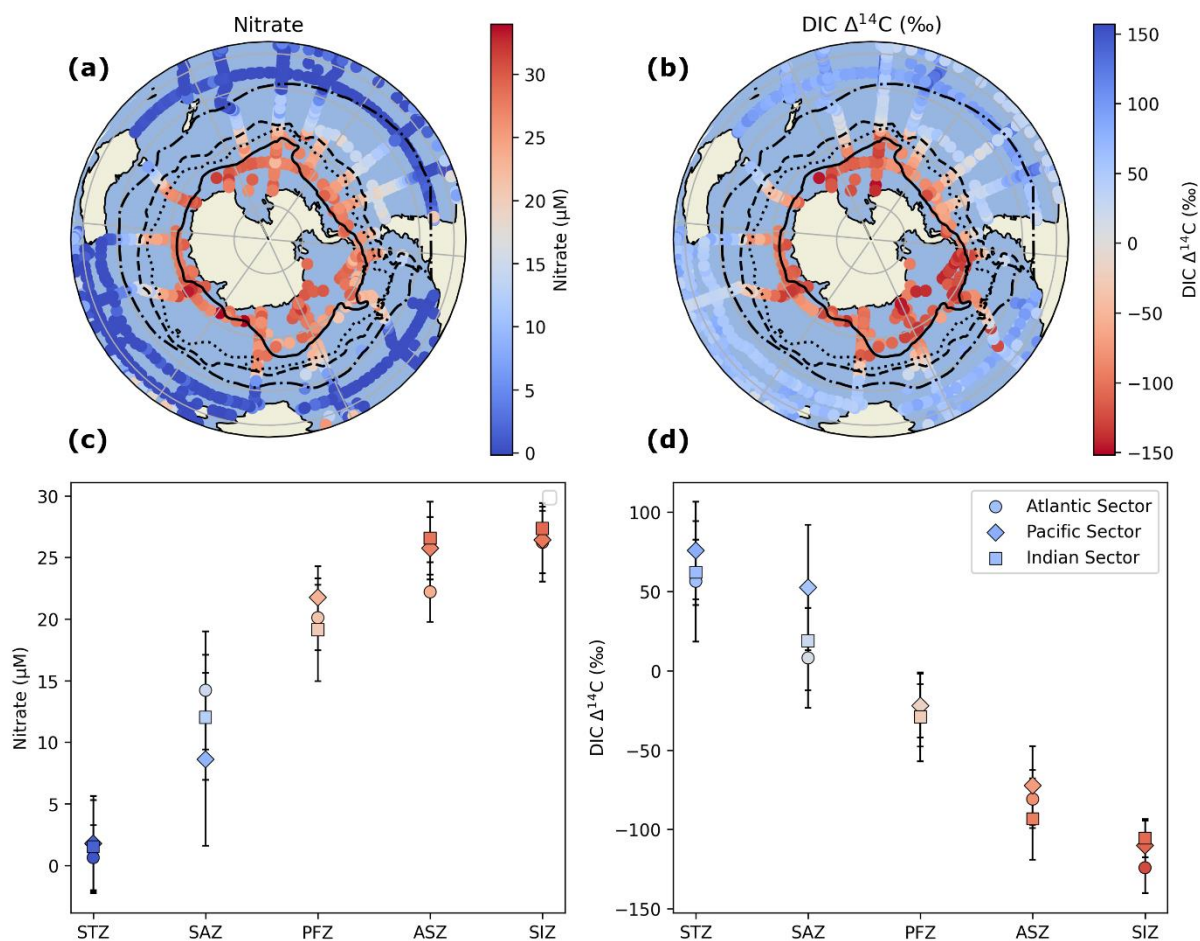
300   **Figure 6: (a/b) Nitrate and DIC Δ^{14}C data from GLODAP Merged and Adjusted Data Product v2.2023 (Key et al., 2004; Lauvset et al., 2023; Olsen et al., 2016). Data were filtered for measurements south of 5S, and depths 0-100m, after 1980. (c/d) The mean and 1-σ standard deviation of nitrate DIC Δ^{14}C for each ACC zone (zones from Orsi et al., 1995, Gray et al., 2018).**

305   The meridional extent of the different Southern Ocean zones vary longitudinally, and this may have an impact on

tree-ring $\Delta^{14}CO_2$. The New Zealand tree-ring sites necessarily have a shorter meridional range (41.1°S to 52.5°S) than Chilean

sites (extending to 54.9°S), but a larger proportion of New Zealand back-trajectories lie in the crucial year-round outgassing

ASZ because the zone is expanded in the Indian Ocean sector relative to Pacific. The ASZ surface also has lower Δ^{14}C than

more northerly zones (Fig 6d) amplifying the effect of atmospheric dilution of ^{14}C relative to outgassing in general. (Prend et

310   al., 2022) discovered a deep maximum mixed layer depth surrounding Campbell Island and westward in the ASZ (Prend 2022 Fig 1c) which corresponds well with Campbell Island's HYSPLIT back-trajectory plume core (Fig 4(a)). This phenomenon was found in ARGO data from 2000-2020, and therefore isn't representative of the entirety of our time-series which spans from 1980 to 2017. Low $\Delta\Delta^{14}CO_2$ at Campbell Island may be linked air originating in strong upwelling zones in the Indian Ocean, but also local effects such as a deep mixing and obduction leading to strong fluxes directly west of Campbell Island.

315   **4 Conclusion**

While other methods of estimating Southern Ocean air-sea CO_2 flux face the challenge of distinguishing between two large opposing forces (outgassing of natural CO_2 and uptake of natural CO_2), radiocarbon measurements through long-term atmospheric records (Levin et al., 2010) or tree-rings allow us to constrain a one-way flux by measuring dilution of atmospheric radiocarbon from outgassing of CO_2 from aged water masses. They also provide the opportunity to reconstruct changes in the

320   past when hydrographic and float-based data were sparse. We report a novel database of 438 unique tree ring Δ^{14}C measurements from Chile and New Zealand from 1980-2016. This work substantially expands the Δ^{14}C records from the Southern mid-high latitudes and is consistent with previous studies that demonstrate the imprint of Southern Ocean upwelling on atmospheric Δ^{14}C in the Southern Hemisphere (Levin et al., 2010; Graven et al., 2012). The upwelling signal is most apparent at Campbell Island, the southernmost New Zealand site that has HYSPLIT back-trajectory footprints in the ASZ, the

325   only ocean zone to exhibit year-round outgassing (Gray et al., 2018). The link between low $\Delta\Delta^{14}CO_2$ in Campbell Island tree-rings, air mass origination in the Indian Sector ASZ, and local effects such as nearby obduction from deep mixed layer (Prend et al., 2022) should be further explored for viability as a proxy for detecting changes in upwelling.

Data at more northerly sites and those that are influenced by air masses from lower-latitude ocean zones appear fairly homogenous. This suggests that the influence of non-local fossil fuel and biospheric signals are small in the Southern

330   Hemisphere. Further investigation is required to understand the mechanism behind low values at Chilean site Monte Tarn, and if fossil fuel contamination from a nearby shipping lane may play a role.

Tree-ring Δ^{14}C measurements are key tools to reconstruct atmospheric Δ^{14}C and may provide new opportunities when trying to understand changes in Southern Ocean upwelling, and air-sea CO_2 flux. This work also highlights the potential for ship-based atmospheric Δ^{14}C measurements to detect changes in ocean upwelling. Ship-based atmospheric Δ^{14}C samples can

335   be collected with higher temporal frequency, without the need for oceanographic research vessels. More investigation is required to understand *temporal* changes in $\Delta\Delta^{14}CO_2$. In a companion work to follow, we will address trends over time and analyse how our trends compare with (Le Quéré et al., 2007) and ocean model output.

340

5 Code availability

Scripts used to create this work can be found in the GitHub directory below. Supplemental Materials includes a detailed list

345 of the job each script performs in the data-analysis workflow. The GitHub page also includes a list of dependencies required

for the scripts to function.

https://github.com/christianlewis091/science_projects/tree/main/soar_tree_rings/scripts_EGU_submission

6 Data availability

350 Tree ring Δ^{14}C measurements (Fig. 2 (e/f)), mean $\Delta\Delta^{14}CO_2$ (Fig. 3), results from HYSPLIT back-trajectory modelling (Fig.

5), and summary results from GLODAP analyses (Fig. 6) are available at 10.5281/zenodo.14532802 in .xlsx format.

Comments above data on each tab reference codes in GitHub directory described above. Data used for GLODAP analysis is

publicly available at https://glodap.info/index.php/merged-and-adjusted-data-product-v2-2023/. Baring Head atmospheric

time series data can be found as described in Data Availability statement in (Turnbull et al., 2017), and Cape Grim time

355 series data described in (Levin et al., 2010).

7 Supplement

Supplemental material is available online at {link to be determined after submission}.

8 Author contributions

360 **RC:** conceptualization, sample collection, sample processing, analysis and writing; **SMF** and **EB**: analysis and

interpretation, methodology, and writing; **RM** and **GB**: maintenance and sample curation from Baring Head Atmospheric

Research Station and site-site intercomparison; **AL**: administration, methods, and supervision of tree-ring processing, **MN**:

administration. methodology, resources, writing; **CBL**: formal analysis, investigation, methodology, software, validation,

365 visualization, writing; **JT**: funding acquisition, conceptualization and data curation, analysis, methodology, supervision and

writing. All authors were involved in reviewing and editing the manuscript.

9 Competing Interests

The authors declare that they have no conflict of interest.

10 Acknowledgements

370

References

Ancapichún, Santiago, et al. "Radiocarbon bomb-peak signal in tree-rings from the tropical Andes register low latitude
atmospheric dynamics in the Southern Hemisphere." *Science of the Total Environment* 774 (2021): 145126.
385

Ancapichun, S., De Pol-Holz, R., Christie, D. A., Santos, G. M., Collado-Fabbri, S., Garreaud, R., Lambert, F., Orfanoz-
Cheuquelaf, A., Rojas, M., Southon, J., Turnbull, J. C., & Creasman, P. P. (2021). Radiocarbon bomb-peak signal in tree-
rings from the tropical Andes register low latitude atmospheric dynamics in the Southern Hemisphere. *Sci Total Environ*,
774, 145126. https://doi.org/10.1016/j.scitotenv.2021.145126
390

Anderson, R. F., Ali, S., Bradtmiller, L. I., Nielsen, S. H. H., Fleisher, M. Q., Anderson, B. E., & Burckle, L. H. (2009).
Wind-Driven Upwelling in the Southern Ocean and the Deglacial Rise in Atmospheric CO_2. *Science*, *323*(5920), 1443–1448.
https://doi.org/10.1126/science.1167441

395 Andreu-Hayles, L., Santos, G. M., Herrera-Ramírez, D. A., Martin-Fernández, J., Ruiz-Carrascal, D., Boza-Espinoza, T. E.,
Fuentes, A. F., & J∅rgensen, P. M. (2015). Matching Dendrochronological Dates with the Southern Hemisphere [14]C Bomb
Curve to Confirm Annual Tree Rings in *Pseudolmedia rigida* from Bolivia. *Radiocarbon*, *57*(1), 1–13.
https://doi.org/10.2458/azu_rc.57.18192

Crotwell AM, Lee H, Steinbacher M. 2020. 20th WMO/IAEA Meeting on Carbon Dioxide, Other Greenhouse Gases and
400 Related Measurement Techniques (GGMT-2019). World Meteorological Organization. No. GAW Report No. 255.

Chen, H., Haumann, F. A., Talley, L. D., Johnson, K. S., & Sarmiento, J. L. (2022). The Deep Ocean's Carbon Exhaust.
Global Biogeochem Cycles, *36*(7), Article 7. https://doi.org/10.1029/2021GB007156

405 Corran, R. (2021). *Tree Ring Reconstruction Of Modern Radiocarbon Dioxide Variability Over The Southern
Ocean* (Doctoral dissertation, Open Access Te Herenga Waka-Victoria University of Wellington).

DeVries, T. (2014). The oceanic anthropogenic CO2 sink: Storage, air-sea fluxes, and transports over the industrial
era. *Global Biogeochemical Cycles*, *28*(7), 631-647.

410   DeVries, T., Holzer, M., & Primeau, F. (2017). Recent increase in oceanic carbon uptake driven by weaker upper-ocean overturning. *Nature*, *542*(7640), 215-218.

Fay, A. R., McKinley, G. A., & Lovenduski, N. S. (2014). Southern Ocean carbon trends: Sensitivity to methods. *Geophysical Research Letters*, *41*(19), 6833–6840. https://doi.org/10.1002/2014GL061324

415   Fong, M. B., & Dickson, A. G. (2019). Insights from GO-SHIP hydrography data into the thermodynamic consistency of CO2 system measurements in seawater. *Marine Chemistry*, *211*, 52–63. https://doi.org/10.1016/j.marchem.2019.03.006

Fröhlicher, T. L., Sarmiento, J. L., Paynter, D. J., Dunne, J. P., Krasting, J. P., & Winton, M. (2015). Dominance of the Southern Ocean in Anthropogenic Carbon and Heat Uptake in CMIP5 Models. *Journal of Climate*, *28*(2), 862–886. https://doi.org/10.1175/jcli-d-14-00117.1

420   Graven, H. D., Gruber, N., Key, R., Khatiwala, S., & Giraud, X. (2012). Changing controls on oceanic radiocarbon: New insights on shallow-to-deep ocean exchange and anthropogenic CO2uptake. *Journal of Geophysical Research: Oceans*, *117*(C10), n/a-n/a. https://doi.org/10.1029/2012jc008074

Graven, H. D., Guilderson, T. P., & Keeling, R. F. (2007). Methods for High-Precision ^{14}C AMS Measurement of Atmospheric CO$_2$ at LLNL. *Radiocarbon*, *49*(2), 349–356. https://doi.org/10.1017/S0033822200042284

425   Gray, A. R., Johnson, K. S., Bushinsky, S. M., Riser, S. C., Russell, J. L., Talley, L. D., Wanninkhof, R., Williams, N. L., & Sarmiento, J. L. (2018). Autonomous Biogeochemical Floats Detect Significant Carbon Dioxide Outgassing in the High-Latitude Southern Ocean. *Geophysical Research Letters*, *45*(17), 9049–9057. https://doi.org/10.1029/2018gl078013

Gruber, N., Bakker, D. C. E., DeVries, T., Gregor, L., Hauck, J., Landschützer, P., McKinley, G. A., & Müller, J. D. (2023). Trends and variability in the ocean carbon sink. *Nature Reviews Earth & Environment*, *4*(2), 119–134.
430   https://doi.org/10.1038/s43017-022-00381-x

Gruber, N., Gloor, M., Mikaloff Fletcher, S. E., Doney, S. C., Dutkiewicz, S., Follows, M. J., Gerber, M., Jacobson, A. R., Joos, F., Lindsay, K., Menemenlis, D., Mouchet, A., Müller, S. A., Sarmiento, J. L., & Takahashi, T. (2009). Oceanic sources, sinks, and transport of atmospheric CO$_2$. *Global Biogeochemical Cycles*, *23*(1), 2008GB003349. https://doi.org/10.1029/2008GB003349

435   Gruber, N., Landschutzer, P., & Lovenduski, N. S. (2019). The Variable Southern Ocean Carbon Sink. *Ann Rev Mar Sci*, *11*, 159–186. https://doi.org/10.1146/annurev-marine-121916-063407

Hauck, J., Gregor, L., Nissen, C., Patara, L., Hague, M., Mongwe, P., Bushinsky, S., Doney, S. C., Gruber, N., Le Quéré, C., Manizza, M., Mazloff, M., Monteiro, P. M. S., & Terhaar, J. (2023). The Southern Ocean Carbon Cycle 1985–2018: Mean, Seasonal Cycle, Trends, and Storage. *Global Biogeochemical Cycles*, *37*(11), e2023GB007848.
440   https://doi.org/10.1029/2023GB007848

Hua, Q., Barbetti, M., & Rakowski, A. Z. (2013). Atmospheric Radiocarbon for the Period 1950–2010. *Radiocarbon*, *55*(4), 2059–2072. https://doi.org/10.2458/azu_js_rc.v55i2.16177

Hua, Q., Barbetti, M., Worbes, M., Head, J., & Levchenko, V. A. (1999). Review of Radiocarbon Data from Atmospheric and Tree Ring Samples for the Period 1945-1997 Ad. *IAWA Journal*, *20*(3), 261–283. https://doi.org/10.1163/22941932-
445   90000690

Hua, Q., Turnbull, J. C., Santos, G. M., Rakowski, A. Z., Ancapichún, S., De Pol-Holz, R., Hammer, S., Lehman, S. J.,
Levin, I., Miller, J. B., Palmer, J. G., & Turney, C. S. M. (2021). Atmospheric Radiocarbon for the Period 1950–2019.
Radiocarbon, *64*(4), 723–745. https://doi.org/10.1017/rdc.2021.95

450   Key, R. M., Kozyr, A., Sabine, C. L., Lee, K., Wanninkhof, R., Bullister, J. L., Feely, R. A., Millero, F. J., Mordy, C., &
Peng, T. -H. (2004). A global ocean carbon climatology: Results from Global Data Analysis Project (GLODAP). *Global
Biogeochemical Cycles*, *18*(4), 2004GB002247. https://doi.org/10.1029/2004GB002247

Kromer, B., & Munnich, K. O. (1992). CO2 gas proportional counting in radiocarbon dating—Review and perspective.
Radiocarbon After Four Decades.

455   Lauvset, S. K., Key, R. M., Olsen, A., Van Heuven, S. M. A. C., Velo, A., Lin, X., Schirnick, C., Kozyr, A., Tanhua, T.,
Hoppema, M., Jutterström, S., Steinfeldt, R., Jeansson, E., Ishii, M., Pérez, F. F., Suzuki, T., & Watelet, S. (2023). *A new
global interior ocean mapped climatology: The 1° × 1° GLODAP version 2 from 1972-01-01 to 2013-12-31 (NCEI
Accession 0286118)* [Dataset]. NOAA National Centers for Environmental Information.
https://doi.org/10.3334/CDIAC/OTG.NDP093_GLODAPV2

460   Le Quéré, C., Rödenbeck, C., Buitenhuis, E. T., Conway, T. J., Langenfelds, R., Gomez, A., Labuschagne, C., Ramonet, M.,
Nakazawa, T., Metzl, N., Gillett, N., & Heimann, M. (2007). Saturation of the Southern Ocean CO2 Sink Due to Recent
Climate Change. *Science*, *316*(5832), 1735–1738. https://doi.org/10.1126/science.1136188

Leavitt, S. W., & Bannister, B. (2009). Dendrochronology and Radiocarbon Dating: The Laboratory of Tree-Ring Research
Connection. *Radiocarbon*, *51*(1), 373–384. https://doi.org/10.1017/S0033822200033889

465   Levin, I., Naegler, T., Kromer, B., Diehl, M., Francey, R. J., Gomez-Pelaez, A. J., Steele, L. P., Wagenbach, D., Weller, R.,
& Worthy, D. E. (2010). Observations and modelling of the global distribution and long-term trend of atmospheric $^{14}CO_2$.
Tellus B: Chemical and Physical Meteorology, *62*(1). https://doi.org/10.1111/j.1600-0889.2009.00446.x

Long, M. C., Stephens, B. B., McKain, K., Sweeney, C., Keeling, R. F., Kort, E. A., Morgan, E. J., Bent, J. D., Chandra, N.,
Chevallier, F., Commane, R., Daube, B. C., Krummel, P. B., Loh, Z., Luijkx, I. T., Munro, D., Patra, P., Peters, W.,
Ramonet, M., … Wofsy, S. C. (2021). Strong Southern Ocean carbon uptake evident in airborne observations. *Science*,
470   *374*(6572), 1275–1280. https://doi.org/10.1126/science.abi4355

Lovenduski, N. S., Gruber, N., & Doney, S. C. (2008). Toward a mechanistic understanding of the decadal trends in the
Southern Ocean carbon sink. *Global Biogeochemical Cycles*, *22*(3). https://doi.org/10.1029/2007gb003139

Marinov, I., Gnanadesikan, A., Toggweiler, J. R., & Sarmiento, J. L. (2006). The Southern Ocean biogeochemical divide.
Nature, *441*(7096), 964–967. https://doi.org/10.1038/nature04883

475   McNichol, A. P., Key, R. M., & Guilderson, T. P. (2022). GLOBAL OCEAN RADIOCARBON PROGRAMS.
Radiocarbon, *64*(4), 675–687. https://doi.org/10.1017/RDC.2022.17

Mikaloff Fletcher, S. E., Gruber, N., Jacobson, A. R., Doney, S. C., Dutkiewicz, S., Gerber, M., Follows, M., Joos, F.,
Lindsay, K., Menemenlis, D., Mouchet, A., Müller, S. A., & Sarmiento, J. L. (2006). Inverse estimates of anthropogenic
CO2 uptake, transport, and storage by the ocean. *Global Biogeochemical Cycles*, *20*(2).
480   https://doi.org/10.1029/2005gb002530

Millissa S. C. Warner. (2018). Introduction to PySPLIT A Python Toolkit for NOAA ARLs HYSPLIT Model. *Computing in
Science and Engineering*.

Naegler, T., & Levin, I. (2009). Biosphere-atmosphere gross carbon exchange flux and the $\delta^{13}CO_2$ and $\Delta^{14}CO_2$ disequilibria constrained by the biospheric excess radiocarbon inventory. *Journal of Geophysical Research: Atmospheres*, *114*(D17), 2008JD011116. https://doi.org/10.1029/2008JD011116

Nevison, C. D., Manizza, M., Keeling, R. F., Stephens, B. B., Bent, J. D., Dunne, J., Ilyina, T., Long, M., Resplandy, L., Tjiputra, J., & Yukimoto, S. (2016). Evaluating CMIP5 ocean biogeochemistry and Southern Ocean carbon uptake using atmospheric potential oxygen: Present-day performance and future projection. *Geophysical Research Letters*, *43*(5), 2077–2085. https://doi.org/10.1002/2015gl067584

Norris, M. W. (2015). *Reconstruction of historic fossil CO2 emissions using radiocarbon measurements from tree rings.*

Olsen, A., Key, R. M., Van Heuven, S., Lauvset, S. K., Velo, A., Lin, X., Schirnick, C., Kozyr, A., Tanhua, T., Hoppema, M., Jutterström, S., Steinfeldt, R., Jeansson, E., Ishii, M., Pérez, F. F., & Suzuki, T. (2016). The Global Ocean Data Analysis Project version 2 (GLODAPv2) – an internallyconsistent data product for the world ocean. *Earth System Science Data*, *8*(2), 297–323. https://doi.org/10.5194/essd-8-297-2016

Orsi, A.H, Whitworth, T, & Nowlin Jr W.D. (1995). On the meridional extent and fronts of the Antarctic Circumpolar Current. *Deep-Sea Research*, *42*, 641–673.

Peter Landschutzer, N. G. (2015). The reinvigoration of the Southern Ocean carbon sink. *Science*, *349*(6253).

Prend, C. J., Gray, A. R., Talley, L. D., Gille, S. T., Haumann, F. A., Johnson, K. S., Riser, S. C., Rosso, I., Sauvé, J., & Sarmiento, J. L. (2022). Indo-Pacific Sector Dominates Southern Ocean Carbon Outgassing. *Global Biogeochemical Cycles*, *36*(7), Article 7. https://doi.org/10.1029/2021gb007226

Randerson, J. T., Enting, I. G., Schuur, E. A. G., Caldeira, K., & Fung, I. Y. (2002). Seasonal and latitudinal variability of troposphere $\Delta^{14}CO_2$: Post bomb contributions from fossil fuels, oceans, the stratosphere, and the terrestrial biosphere. *Global Biogeochemical Cycles*, *16*(4). https://doi.org/10.1029/2002GB001876

Reimer, P. J., Baillie, M. G. L., Bard, E., Bayliss, A., Beck, J. W., Blackwell, P. G., Bronk Ramsey, C., Buck, C. E., Burr, G. S., Edwards, R. L., Friedrich, M., Grootes, P. M., Guilderson, T. P., Hajdas, I., Heaton, T. J., Hogg, A. G., Hughen, K. A., Kaiser, K. F., Kromer, B., … Weyhenmeyer, C. E. (2009). IntCal09 and Marine09 Radiocarbon Age Calibration Curves, 0–50,000 Years cal BP. *Radiocarbon*, *51*(4), 1111–1150. https://doi.org/10.1017/S0033822200034202

Reimer, P. J., Bard, E., Bayliss, A., Beck, J. W., Blackwell, P. G., Ramsey, C. B., Buck, C. E., Cheng, H., Edwards, R. L., Friedrich, M., Grootes, P. M., Guilderson, T. P., Haflidason, H., Hajdas, I., Hatté, C., Heaton, T. J., Hoffmann, D. L., Hogg, A. G., Hughen, K. A., … Van Der Plicht, J. (2013). IntCal13 and Marine13 Radiocarbon Age Calibration Curves 0–50,000 Years cal BP. *Radiocarbon*, *55*(4), 1869–1887. https://doi.org/10.2458/azu_js_rc.55.16947

Sallée, J. B., Speer, K. G., & Rintoul, S. R. (2010). Zonally asymmetric response of the Southern Ocean mixed-layer depth to the Southern Annular Mode. *Nature Geoscience*, *3*(4), 273–279. https://doi.org/10.1038/ngeo812

Sarmiento, J. L., Johnson, K. S., Arteaga, L. A., Bushinsky, S. M., Cullen, H. M., Gray, A. R., Hotinski, R. M., Maurer, T. L., Mazloff, M. R., Riser, S. C., Russell, J. L., Schofield, O. M., & Talley, L. D. (2023). The Southern Ocean carbon and climate observations and modeling (SOCCOM) project: A review. *Progress in Oceanography*, *219*. https://doi.org/10.1016/j.pocean.2023.103130

Southon, J., De Pol-Holz, R., & Druffel, E. M. (2016). Paleoclimatology. In *Radiocarbon and Climate Change* (pp. 221–252). Springer.

520   Stuiver, M., & Quay, P. D. (1981). Atmospheric14C changes resulting from fossil fuel CO2 release and cosmic ray flux variability. *Earth and Planetary Science Letters*, *53*(3), 349–362.

Takahashi, T., Sweeney, C., Hales, B., Chipman, D., Newberger, T., Goddard, J., Iannuzzi, R., & Sutherland, S. (2012). The Changing Carbon Cycle in the Southern Ocean. *Oceanography*, *25*(3), 26–37. https://doi.org/10.5670/oceanog.2012.71

Talley, L. D. (2013). Closure of the global overturning circulation through the Indian, Pacific and Southern Oceans:
525   Schematics and transports. *Oceanography*.

Turnbull, J. C., Graven, H., & Krakauer, N. Y. (2016). Radiocarbon in the Atmosphere. In *Radiocarbon and Climate Change*.

Turnbull, J. C., Mikaloff Fletcher, S. E., Ansell, I., Brailsford, G. W., Moss, R. C., Norris, M. W., & Steinkamp, K. (2017). Sixty years of radiocarbon dioxide measurements at Wellington, New Zealand: 1954–2014. *Atmospheric Chemistry and*
530   *Physics*, *17*(23), 14771–14784. https://doi.org/10.5194/acp-17-14771-2017

Ziehn, T., Nickless, A., Rayner, P. J., Law, R. M., Roff, G., & Fraser, P. (2014). Greenhouse gas network design using backward Lagrangian particle dispersion modelling − Part 1: Methodology and Australian test case. *Atmospheric Chemistry and Physics*, *14*(17), 9363–9378. https://doi.org/10.5194/acp-14-9363-2014

Zondervan, A., Hauser, T. M., Kaiser, J., Kitchen, R. L., Turnbull, J. C., & West, J. G. (2015). XCAMS: The compact 14C
535   accelerator mass spectrometer extended for 10Be and 26Al at GNS Science, New Zealand. *Nuclear Instruments and Methods in Physics Research Section B: Beam Interactions with Materials and Atoms*, *361*, 25–33. https://doi.org/10.1016/j.nimb.2015.03.013